Inner Workings of the Hydrazine Synthase Multiprotein Complex

Andreas Dietl[1], Christina Ferousi[2], Wouter J. Maalcke[2], Andreas Menzel[3], Simon de Vries[4], Jan T. Keltjens[2], Mike S.M. Jetten[2, 4], Boran Kartal[2, 5] and Thomas R.M. Barends[1]

1) Department of Biomolecular Mechanisms, Max Planck Institute for Medical Research, 69120 Heidelberg, Germany
2) Department of Microbiology, Institute for Water and Wetland Research, Radboud University Nijmegen, 6525 AJ Nijmegen, the Netherlands
3) Swiss Light Source, Paul Scherrer Institute, 5232 Villigen, Switzerland
4) Department of Biotechnology, Delft University of Technology, Delft, the Netherlands
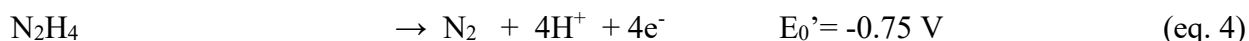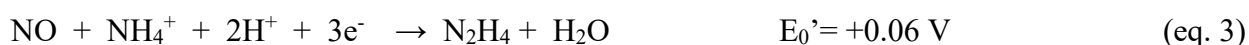*5) Department of Biochemistry and Microbiology, Laboratory of Microbiology, Gent University, Gent, Belgium.*

Anaerobic ammonium oxidation (anammox) plays a major role in the earth's nitrogen cycle[1,2] and is used in energy-efficient wastewater treatment[3]. This bacterial process combines nitrite and ammonium forming dinitrogen gas, and has been estimated to synthesize up to 50% of the dinitrogen gas emitted into our atmosphere from the oceans[2]. Strikingly, the anammox process relies on the highly unusual, extremely reactive intermediate hydrazine[4], a compound also used as a rocket fuel because of its high reducing power. So far, the enzymatic mechanism by which hydrazine is synthesized is unknown. Here we report the 2.7 Å resolution crystal structure as well as biophysical and spectroscopic studies of a hydrazine synthase multiprotein complex isolated from the anammox organism *Kuenenia stuttgartiensis*. The structure shows an elongated dimer of heterotrimers, each of which has two unique *c*-type heme-containing active sites, as well an interaction point for a redox partner. Furthermore, a system of tunnels connects these active sites. The crystal structure implies a two-step mechanism for hydrazine synthesis: a three-electron reduction of nitric oxide to hydroxylamine at the active site of the γ-subunit and its subsequent condensation with ammonia yielding hydrazine in the active centre of the α-subunit. Our results provide the first, detailed structural insight into the mechanism of biological hydrazine synthesis, which is of major significance for our understanding of the conversion of nitrogenous compounds in nature.

1

Most nitrogen on earth occurs as gaseous N_2 (nitrogen oxidation number 0). To make nitrogen available for biochemical reactions, the inert N_2 has to be converted to ammonia (oxidation number -III), which can then be assimilated to produce organic nitrogen compounds, or be oxidized to nitrite (oxidation number +III) or nitrate (+V). The reduction of nitrite in turn results in the regeneration of N_2, thus closing the biological nitrogen cycle.

To produce N_2 from nitrite, a nitrogen-nitrogen bond must be formed by the addition of another nitrogen-containing molecule. At present, two biological processes are known that achieve this. In denitrification, nitrite is first reduced to nitric oxide (NO, +II). Then, two molecules of NO are combined to produce nitrous oxide (N_2O, +I), which is subsequently reduced to N_2. The other process, anaerobic ammonium oxidation or anammox[1,2], was discovered only relatively recently, and relies on the combination of two compounds with different nitrogen oxidation states, nitrite and ammonium, to generate N_2.

Our current understanding of the anammox reaction (eq. 1) is based on genomic, physiological and biochemical studies on the anammox bacterium *Kuenenia stuttgartiensis*[4,5]. First, nitrite is reduced to nitric oxide (NO, eq. 2) which is then condensed with ammonium-derived ammonia (NH_3) to yield hydrazine (N_2H_4, eq. 3). Hydrazine itself is a highly unusual metabolic intermediate, as it is extremely reactive and therefore toxic, and has a very low redox potential ($E_0' = -750$ mV). In the final step in the anammox process, it is oxidized to N_2, yielding four electrons (eq. 4) that replenish those needed for nitrite reduction and hydrazine synthesis and are used to establish a proton-motive force across the membrane of the anammox organelle, the anammoxosome, driving ATP synthesis (see[6] for a review).

$NO_2^- + NH_4^+$	$\rightarrow N_2 + 2\ H_2O$	$\Delta G^{0'} = -357$ kJ mol^{-1}	(eq. 1)
$NO_2^- + 2H^+ + e^-$	$\rightarrow NO + H_2O$	$E_0' = +0.38$ V	(eq. 2)
$NO + NH_4^+ + 2H^+ + 3e^-$	$\rightarrow N_2H_4 + H_2O$	$E_0' = +0.06$ V	(eq. 3)
N_2H_4	$\rightarrow N_2 + 4H^+ + 4e^-$	$E_0' = -0.75$ V	(eq. 4)

The enzyme producing hydrazine from NO and ammonium – hydrazine synthase (HZS) – is biochemically unique. A complex of three proteins, HZS α, -β and –γ, encoded by the genes *kuste2861*, *-2859* and *-2860*, respectively, was put forward as the probable hydrazine synthase enzyme[5]. This complex was isolated from *Kuenenia* cells and shown to be catalytically active in a coupled assay with the octaheme *c*-type cytochrome kustc1061[7] to convert hydrazine into N_2 and return electrons to HZS[4]. Isolated HZS is a comparatively slow enzyme with an activity of 20 nmol

h^{-1} mg^{-1} protein, about 1% of *in vivo* turnover. This dramatic loss of activity occurs immediately upon cell lysis and might be explained by the disruption of a tightly coupled multicomponent system, as well as by the use of bovine cytochrome *c* as an artificial electron carrier in the *in vitro* assay[4].

Using a custom-designed crystal cooling method, we prepared well diffracting crystals of the HZS αβγ multienzyme complex from *Kuenenia stuttgartiensis* without substrates and determined its crystal structure at 2.7 Å resolution in the absence of substrates (Fig. 1a, Extended Data Table 1). The structure reveals a crescent-shaped dimer of heterotrimers with an (αβγ)$_2$ stoichiometry. The overall size and shape of the complex are confirmed by analytical ultracentrifugation and solution small-angle X-ray scattering (Supplemental information, Extended Data Fig. 1). Each heterotrimer contains four hemes and one zinc ion as well as several calcium ions (Fig. 1b, Supplemental Information, Extended data Table 2).

The α-subunit (Fig. 1c) consists of three domains: an N-terminal domain which includes a six-bladed β-propeller, a middle domain binding a pentacoordinated *c*-type heme (heme αI) and a C-terminal domain which harbors a bis-histidine-coordinated *c*-type heme (heme αII). The structure around heme αI (Fig. 1d) deviates significantly from a typical heme *c* site, as the canonical histidine of the heme *c* binding motif, αHis587, is rotated away from the heme iron, and coordinates a zinc ion. Instead, the hydroxyl group of αTyr591 serves as the proximal ligand to the heme iron, as in the active site of many catalases[8]. Importantly, this tyrosine is conserved in HZS α sequences (Extended Data Fig. 2). The zinc bound to αHis587 is further coordinated by one of the heme αI propionate groups as well as αCys303 and likely a water molecule, in a structure reminiscent of the active sites of alcohol dehydrogenase and various metalloproteases[9]. The zinc ion could play a structural role, assisting in rotating αHis587 away from the iron, allowing αTyr591 to bind, or could directly modulate the chemistry of the heme group, with which it interacts *via* a propionate group. αThr571, αAla569 and αMet556 (which is partially oxidized, see Supplemental Information) are in close proximity to the distal side of heme αI, which does not seem to coordinate a solvent molecule in the crystal structure. In contrast, heme αII is bound by a canonical heme *c* binding motif and is coordinated by αHis772 distally and αHis689 proximally. The edge-to-edge distance[10] between hemes αI and αII is 31 Å (Fig. 1b), which is too long for single-step electron transfer between the heme groups of the α-subunit. The edge-to-edge distances between the heme

groups in the two different α-subunits in the complex are larger than 38 Å, which excludes electron transfer between the two α-subunits on the timescale of catalysis.

The non-heme β-subunit (Fig. 2a) is a seven-bladed β-propeller with a short helical insertion in the sixth propeller blade. The outer strand of the C-terminal blade consists of the N-terminus (residues γ40-γ52) of the γ-subunit of the same heterotrimer. Notably, the HZS β- and γ-subunits are fused into a single polypeptide in the anammox bacteria *Scalindua profunda* and *Scalindua brodae* (Ref. [11], Extended Data Fig. 3).

The structure of the γ-subunit (Fig. 2b) is reminiscent of the fold of the homologous diheme cytochrome *c* peroxidases (CCPs)[12-14] and *Paracoccus denitrificans* Methylamine utilization protein (MauG)[15] and consists of two α-helical lobes, each of which contains one *c*-type heme. Heme γI in the N-terminal lobe (Fig. 2c) is coordinated proximally by γHis106 and distally by a water, and is covalently bound to γCys102 and γCys105 on a typical heme *c* binding motif. Intriguingly, the electron density maps clearly show a unique third covalent bond with the protein, between the C_1 porphyrin methyl group and the Sγ atom of γCys165 (Extended Data Fig. 4a), which possibly serves to modulate heme chemistry. At the distal side, the iron binds a water molecule, which is hydrogen bonded to γAsp168. This conserved residue (Extended Data Fig. 3) is perfectly positioned to transfer protons to a ligand molecule coordinated to the heme. A structural superposition (Extended Data Fig. 4b) reveals that heme γI is located at the position of the high-spin heme of the homologous *Nitrosomonas europaea* CCP[13] and *P. denitrificans* MauG[15].

The bis-His-coordinated heme γII in the C-terminal lobe is located at the equivalent position as the electron transfer heme in CCPs and MauG (Extended Data Fig. 4b), at an edge-to-edge distance of 15 Å from heme γI (Figure 1b), which would allow direct electron transfer between the hemes in the γ-subunit. In CCPs and MauG, a conserved Trp residue is believed to be involved in catalytic redox chemistry. In HZS γ, the position of this tryptophan is taken up by γHis144. The γ-subunit binds three calcium ions, one of them at the same position as the Ca-binding site in CCP that is essential for its activation. Moreover, heme γII is located on the surface of the complex, exposed to the solvent, surrounded by a negatively charged patch, as in a cytochrome *c* binding site (Extended Data Fig. 5). Therefore, heme γII likely functions in electron transfer.

Thus, it appears that the α- and the γ-subunit each contain an active site (hemes αI and γI) and that the γ-subunit contains an electron-transfer site (heme γII). Electron paramagnetic resonance (EPR) spectroscopy (Extended Data Fig. 6, Supplemental Information) is consistent with a stoichiometry of two bis-His coordinated hemes and two hemes for which a population of ligation states exist.

Intriguingly, our crystal structure revealed a tunnel connecting the heme αI and –γI sites (Figure 3a). This tunnel branches off towards the surface of the protein approximately halfway between the heme sites, making them accessible to substrates from the solvent. Indeed, binding studies show that heme αI is accessible to xenon (Extended Data Fig. 4c). Interestingly, in between the α- and γ-subunits, the tunnel is approached by a 15-amino acid long loop of the β-subunit (β245-β260), sticking the conserved βGlu253, which binds a magnesium ion, into the tunnel.

These observations allow a mechanism for biological hydrazine synthesis to be proposed (Figure 3b). The presence of two active sites, connected by a tunnel, strongly suggests a mechanism with two half-reactions. HZS combines NO (nitrogen oxidation number +II) and NH_4^+ (N oxidation number -III). To reach the –II oxidation number of the nitrogen atoms in hydrazine, nitric oxide must be reduced. As proposed earlier[6], this could happen in the γ-subunit, resulting in the production of hydroxylamine (NH_2OH; nitrogen oxidation number –I) according to equation 5.

$$\overset{+II}{NO} + 3H^+ + 3e^- \longrightarrow \overset{-I}{NH_2OH} \qquad \text{(eq. 5)}$$
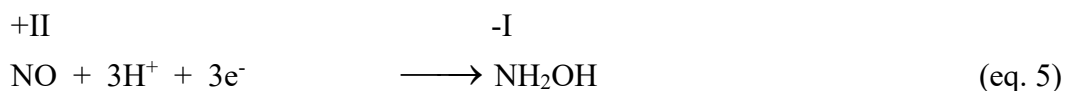
This three-electron reduction is consistent with the proposal that HZS obtains electrons from the triheme cytochrome c kuste2854[6]. In this scheme, the electrons would enter HZS through heme γII and be transferred to the active site heme γI, possibly *via* γHis144. γAsp168 could assist in adding the protons. A cluster of buried, polar residues (γAsp112, γArg143 and γArg167) is positioned between γAsp168 and the surface of the complex and could serve to transfer protons to the active centre of the γ-subunit.

In the proposed mechanism, hydroxylamine then diffuses through the tunnel to the α-subunit's active site. Given the position of the β245-260 loop, the β-subunit could play a role in modulating transport through the tunnel. Hydroxylamine is isoelectronic with hydrogen peroxide, and is a competitive catalase inhibitor[16]. Thus, it would bind to the distal coordination site of the catalase-like heme αI, which would polarize the N-O bond. As crystal soaking with NH_2OH was

unsuccessful, we constructed a model of this complex (Figure 3c) which shows that hydroxylamine would be bound in a tight, very hydrophobic pocket, so that there is little electrostatic shielding of the partial positive charge on the nitrogen. Ammonia produced from ammonium (the predominant form at pH=6.3 in the anammoxosome[17]) could then perform a nucleophilic attack on the nitrogen of hydroxylamine, yielding hydrazine through comproportionation (equation 6).

$$\overset{-I}{NH_2OH} + \overset{-III}{NH_3} \longrightarrow \overset{-II}{N_2H_4} + H_2O \qquad \text{(eq. 6)}$$
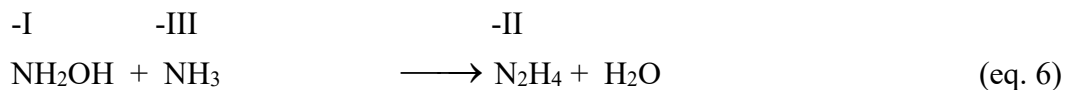
Hydrazine could leave the enzyme *via* the tunnel branch leading to the surface.

Interestingly, the proposed scheme is analogous to the Raschig process used in industrial hydrazine synthesis. There, ammonia is oxidized to chloramine (NH_2Cl, nitrogen oxidation number -I, like in hydroxylamine), which then undergoes comproportionation with another molecule of ammonia to yield hydrazine.
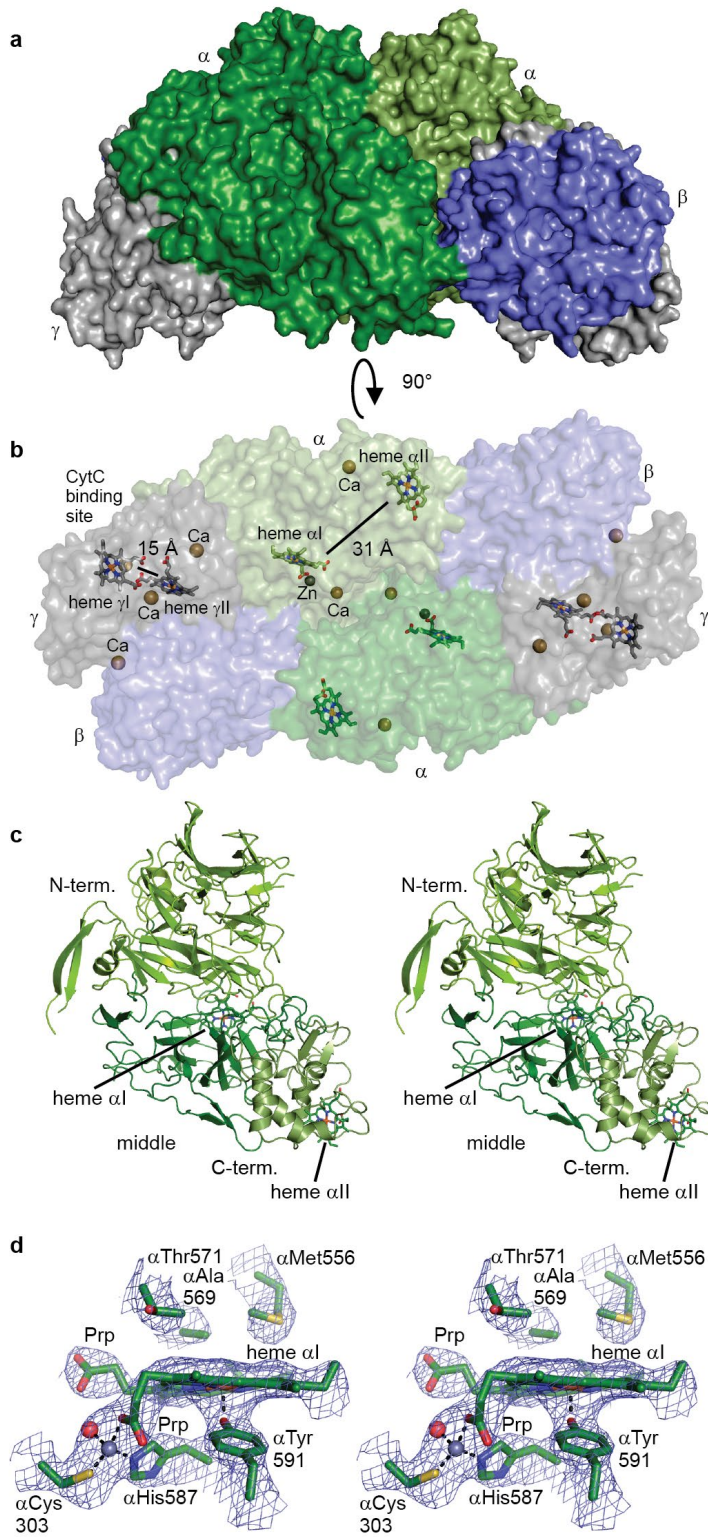
Figures:

Figure 1 | Crystal structure of HZS. a, HZS complex structure; α-subunits are colored green, β-subunits blue and γ-subunits grey. **b**, Surface representation. The contact area between two heterotrimers (~1350 Å^2) is made up of contributions from α- and β-subunits only. Considerable solvent-filled space remains between the heterotrimers. Calcium ions are labeled Ca, zinc as Zn. Edge-to-edge distances between the hemes within a subunit are indicated in Å. **c**, Stereofigure of the α-subunit. The N-terminal domain (residues α28-α420), middle domain (α421-α670) and C-terminal domain (α671-α808) are indicated in different shades of green. The two heme groups are shown as sticks. **d,** Stereofigure of the heme αI site, overlaid with the simulated annealing composite omit map, contoured at 1.0 σ. The zinc ion and its coordinating water are shown as grey and red spheres, respectively. The heme propionates are labeled "Prp".
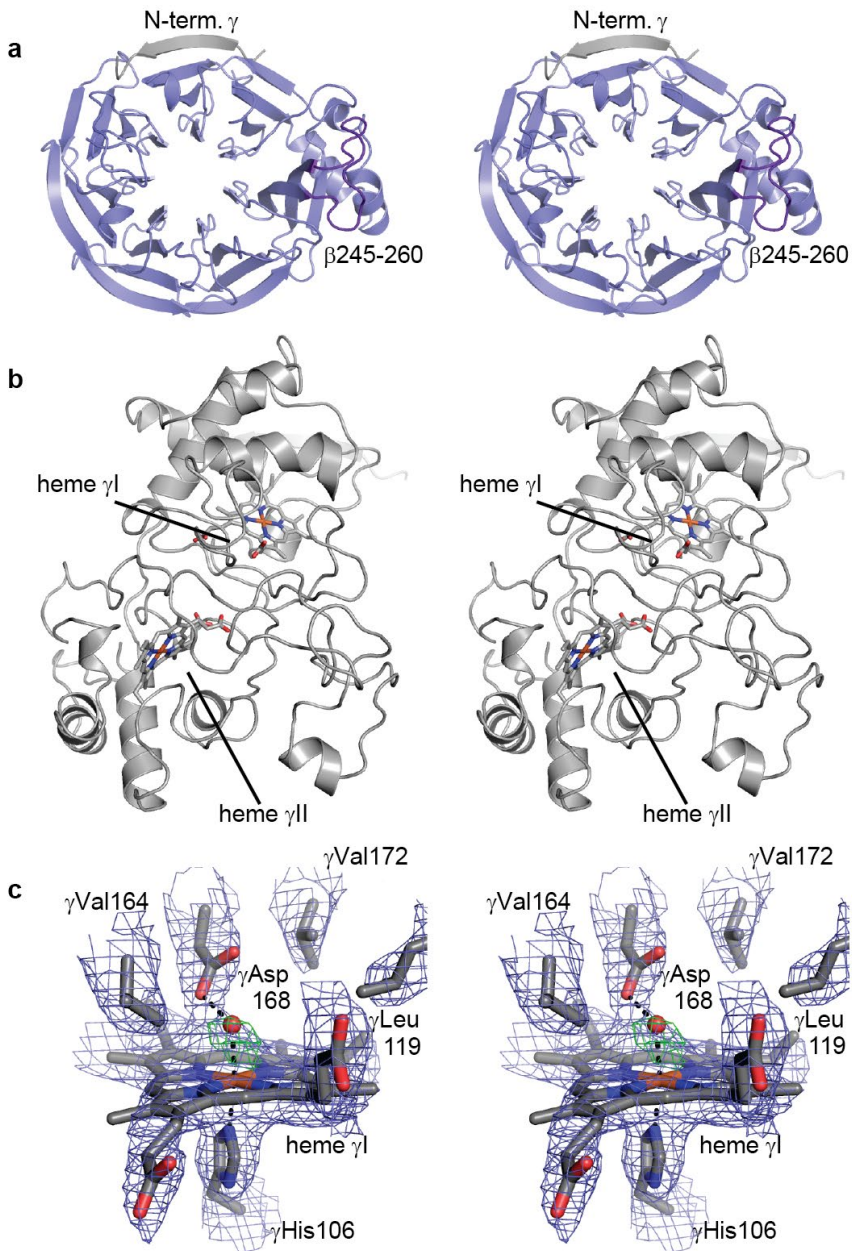
Figure 2 | Structure of HZS β and γ. a, Structure of the β-subunit. The β245-260 insertion is shown in purple. The N-terminus of the γ-subunit, which engages in β-completion with the first blade of the β-propeller is shown in grey. **b**, Structure of the γ-subunit. **c**, Stereofigure of heme γI and its surroundings, overlayed with the simulated annealing composite omit map (blue, 1.0 σ). The water molecule bound to the heme iron is shown as a red sphere. The green mesh is the difference electron density calculated prior to inclusion of the water molecule in the model (5.0 σ).
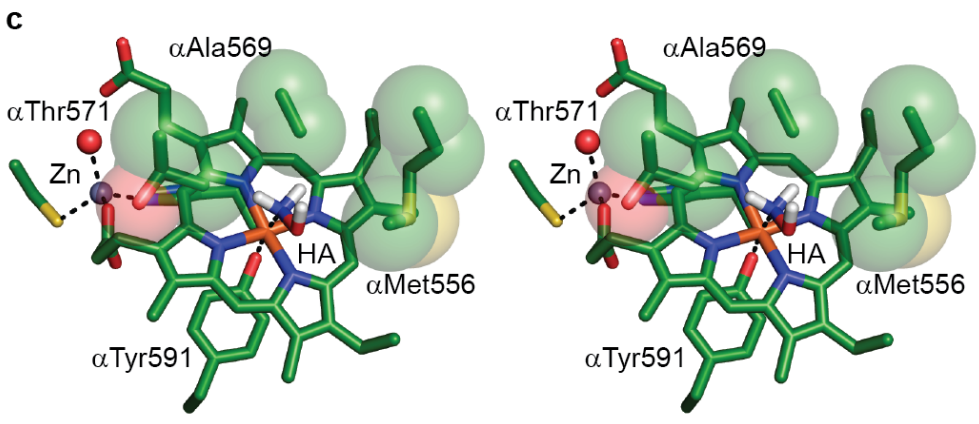
a

to surface

major tunnel

heme γI

β245-260 loop

βGlu253

heme αI

γHis144

Zn

heme γII

γ-subunit

minor tunnel

b

NO

3H⁺

branch to surface

buried polar cluster

major tunnel

α-site reaction:
$NH_2OH + NH_3 \rightarrow N_2H_4 + H_2O$

3e⁻ from redox partner (kuste2854)

NH_2OH

N_2H_4

γAsp168

γHis144

heme γI

3e⁻

NH_3

heme αI

heme γII

γ-site reaction:
$NO+3H^++3e^-\rightarrow NH_2OH$

regulation of tunnel by β245-260 loop

Zn

minor tunnel

NH_3

c

αAla569

αThr571

αAla569

αThr571
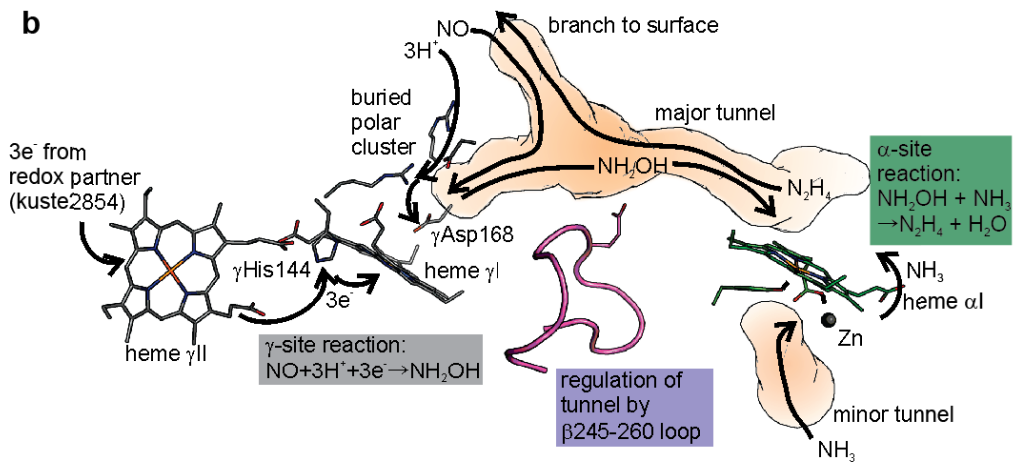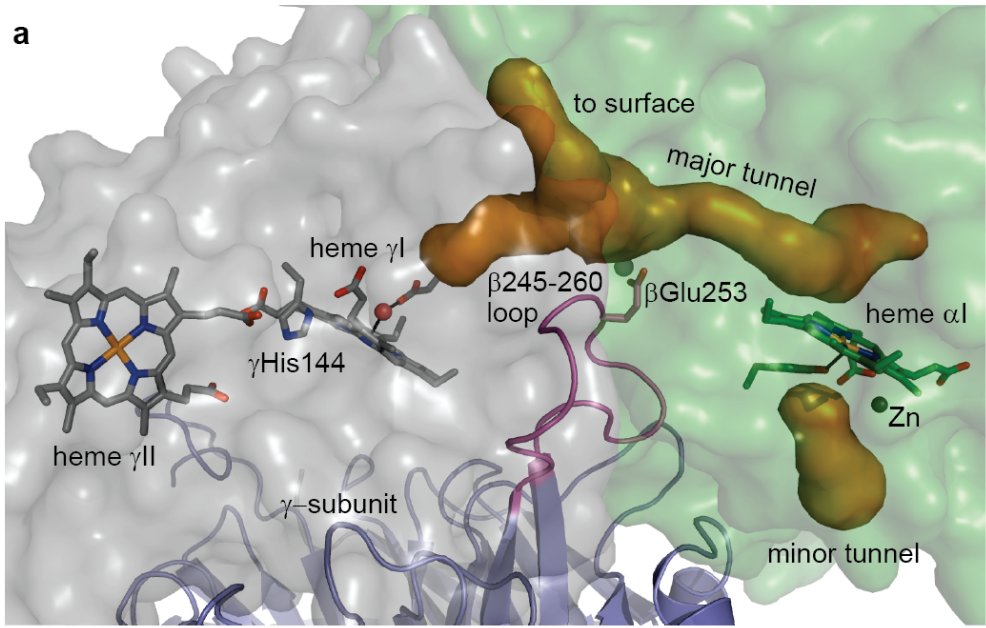
Zn

HA

Zn

HA

αTyr591

αMet556

αTyr591

αMet556

10

Figure 3 | Proposed mechanism of biological hydrazine synthesis. a, Tunnel between the active site hemes (orange, major tunnel) with the branch to the protein surface. The β245-260 loop is shown in purple, as well as βGlu253 which binds a magnesium ion (light green sphere) and γHis144. A minor tunnel (lower right) leads to the zinc ion, and could allow ammonium to enter. **b**, Details of the proposed mechanism. NO travels to heme γI through the tunnel (orange) *via* the branch leading to the surface. On the left, three electrons enter the complex at heme γII and are conducted to heme γI via γHis144. Together with three protons reaching heme γI from the solvent *via* the buried polar cluster, the electrons reduce NO to NH_2OH (grey box). NH_2OH then diffuses through the tunnel, which is regulated by the β-subunit through the β245-260 loop, and binds to heme αI. There, it undergoes comproportionation with NH_3 to yield hydrazine (green box). **c**, Stereofigure, showing a model of hydroxylamine (HA) bound to heme αI in a very hydrophobic environment.

Methods

Protein purification

The kuste2859-2860-2861 hydrazine synthase (HZS) complex was purified from a planktonic *Kuenenia stuttgartiensis* culture as described previously[4]. Briefly, cell-free extracts prepared from a ~95% single-cell enrichment culture of *K. stuttgartiensis* were subjected to ultracentrifugation (180,000×g; 4°C; 1 h) to pellet cell membranes. HZS present in the bright red supernatant was brought to homogeneity by a two-step column purification procedure consisting of subsequent Q Sepharose XL (GE Healthcare) and CHT Ceramic Hydroxyapatite (Bio-Rad, USA) column chromatography steps. UV-Vis spectra of as-isolated HZS showed a Soret absorption peak at 406 nm and a broad band in the 530 nm region, which are typical for fully oxidized (ferric) heme *c* proteins. Reduction of the protein under anoxic conditions using sodium dithionite resulted in a shift of the Soret maximum to 420 nm as well as heme alpha- and beta bands at 553 nm and 523 nm, respectively. Protein concentrations used for ICP-MS and EPR measurements were determined using the Bradford assay (Bio-Rad, USA) with bovine serum albumin as standard.

Analyses by MALDI-TOF and ESI-TOF mass spectrometry

The subunits of the HZS complex were separated by 15% sodium dodecylsulfate polyacrylamide gel-electrophoresis (SDS-PAGE). To identify the individual subunits of the HZS complex, Coomassie-stained SDS gel slices were digested with trypsin or chymotrypsin, followed by reduction with DTT and alkylation with iodoacetamide. The resulting peptides were purified and concentrated using a Millipore ZipTip C-18 column, spotted onto solid targets with α-cyanocinnamic acid, and analyzed by matrix-assisted laser desorption/ionization time-of-flight mass spectrometry (MALDI-TOF MS) on an Axima TOF[2] Performance mass spectrometer (Shimadzu Biotech, Duisburg, Germany). Signal peptide cleavage sites were predicted using the SignalP 3.0 Server[18] applying Hidden-Markov models for Gram-negative bacteria. Liquid HZS samples were analyzed by electrospray ionization time-of-flight mass spectrometry (ESI-TOF MS) on a maXis spectrometer (Bruker Daltonics) under denaturing conditions after diluting in 50% (v/v) acetonitrile/0.1% formic acid and separation by reversed-phase high-performance liquid chromatography (RP-HPLC) using a Discovery BIO Wide Pore C5 column (20 × 2.1 mm, 5 μm particle size, Supelco) at a flow rate of 50 μL/ min.

Metal analysis by inductively-coupled plasma mass spectrometry (ICP-MS)

Metals were analyzed by ICP-MS on a Series I ICP MS (Thermo Scientific, Breda, the Netherlands). Height point calibration was performed with a dilution series of (multi-) element standards (1,000 ppb in 1% nitric acid; Merck, Darmstadt, Germany) using the PlasmaLab software (Thermo Scientific, Breda, the Netherlands). To determine the metal content of HZS, 70-300 µl of purified HZS (26 mg protein/ml) was washed with water using a Vivaspin 500 filter (Sartorius, Göttingen, Germany), destructed with 10% nitric acid at 90°C for 90 min and diluted to 10 ml with water.

Analytical ultracentrifugation (AUC)

Protein samples were concentrated in 25 mM HEPES/KOH, pH 7.5, 25 mM KCl to $A_{280}^{1cm} \approx 0.3$ and $A_{406}^{1cm} \approx 0.45$, corresponding to 0.3 mg/ml, as determined using the Bradford Protein Assay from Bio-Rad. Sedimentation velocity analytical ultracentrifugation was performed in a Beckman ProteomeLab XL-I (Beckmann Coulter GmbH, Krefeld, Germany) analytical ultracentrifuge equipped with an An60Ti rotor at 30,000 rpm and 20°C in a two-sector cell with a 1.2 cm optical path length. Absorption scan data were collected at 280 nm and 406 nm and evaluated using SEDFIT[19].

Protein crystallization and crystal treatment

Hydrazine synthase was concentrated to 45 mg/ml in 25 mM Hepes/KOH pH 7.5, 25 mM KCl by ultrafiltration, divided into 50-µl aliquots , frozen in liquid nitrogen and stored at -80 °C. Prior to crystallization, the protein stock was diluted to 30 mg/ml with 25 mM Hepes/KOH pH 7.5, 25 mM KCl. Crystallization was performed in 1 µL + 1 µL sitting drop vapor-diffusion setups at 4 °C, equilibrating against 500 µL 36% (v/v) 1,4-dioxane. Dark red, rhombohedral crystals with dimensions up to 400×400×100 µm grew within three days. Using PEG 400 or other conventional cryoprotectants, diffraction of these crystals suffered from diffuse scattering, limiting resolution to approx. 4 Å and precluding SAD phasing. Successful cryoprotection was carried out by soaking the crystals for 10-30 seconds in 4 M betaine (N,N,N-trimethylglycine) in 50% (v/v) methanol at 4°C, prior to flash-cooling in liquid nitrogen. These crystals showed sharp Bragg spots, were used for phasing and to build the initial model. However, since the crystals dissolved in the soaking solution at 4°C, crystals were slowly cooled to -20°C on a custom

designed Peltier-cooled microscope stage, which will be described in detail elsewhere. After incubation in the soaking solution at this temperature for up to 30 minutes, crystals were flash cooled in liquid propane at a temperature of approximately 150 K. These crystals diffracted up to 2.7 Å resolution. Xenon treatment was performed in a -20°C room by transferring the crystals cooled to -20°C into a Xe-pressure cell (Xcell, Oxford Cryosystems Ltd., Long Hanborough, UK) and incubating for 5 min at -20°C and a xenon pressure of 20 bar prior to freezing in liquid propane.

X-ray data collection, structure solution and analysis

Diffraction data were collected at beam line X10SA of the Swiss Light Source (Paul Scherrer Institute, Villigen, Switzerland) at 100 K and processed with XDS[20]. A highly redundant single-wavelength anomalous dispersion (SAD) dataset at a resolution of 3.7 Å was collected just above the iron K-edge at a wavelength of 1.735 Å (see Extended data Table 1) which was used for phase determination with AutoSHARP[21]. SHELXD[22] identified 5 heavy atom sites (CC(E)=0.24), which were used by SHARP for phasing, resulting in a figure-of-merit of 0.22. Density modification with SOLOMON[23] resulted in a readily interpretable map, into which the structures of all three subunits could be built using COOT[24]. Phase extension using a dataset of 3.1 Å collected at 0.9763 Å wavelength was carried out with DM[25]. Further refinement against a 2.7 Å data set collected at 1.0000 Å wavelength using PHENIX[26] and REFMAC[27] resulted in a model with good geometry and R-factors (96.4% of residues in favoured regions of the Ramachandran plot, 0.07% Ramachandran outliers, see Extended data Table 1) and revealed that two loop regions in the α-subunit (α175- 177 and α643- 650) where no longer ordered, despite the increase in overall resolution. In order to confirm the identity of the metal sites, datasets above and below the K-edges of iron, copper and zinc were collected (See supplemental information, Extended Data table 2). All other data processing procedures were performed with programs of the CCP4 suite[28]. Tunnels were identified using MOLE 2.0[29] using standard parameters settings starting from αThr571, αTyr591 and γAsp168. Structural figures were prepared using Pymol (Schrödinger). The model of the hydroxylamine complex was prepared by manual docking in COOT[24], using an iron-nitrogen bond length between heme αI and hydroxylamine as observed in crystal structures of catalase/hydroxylamine complexes.

Small-angle X-ray Scattering (SAXS)

Hydrazine Synthase was concentrated to 45 mg/ml in 25 mM HEPES/KOH pH 7.5, 25 mM KCl. SAX data were measured in 1-mm diameter quartz capillaries at the X12SA beam line (cSAXS) of the Swiss Light Source (Paul Scherrer Institute, Villigen, Switzerland) at 283 K. The X-ray photon energy was 12.4 keV, and 200 measurements of 0.5 s each were recorded over 10 positions along the length of the capillary, which was mounted at a detector distance of 2.138 m. Background measurements with the buffer only were taken using the identical capillaries, positions and measurement protocol. Data were used to a maximum momentum transfer of 0.4 $\mathring{A}^{-1}$. Data analysis and three-dimensional reconstruction were performed using the GNOM[30] and GASBOR[31] programs from the ATSAS suite.

EPR spectroscopy

EPR spectroscopy was performed with a Varian E-9 spectrometer operating at X-band (microwave frequency 9.188 GHz; modulation amplitude, 1.0 mT) equipped with a home-made He-flow cryostat at 12 K. HZS samples were used as isolated at a concentration of 205 µM, filled into quartz tubes and shock frozen in liquid nitrogen prior to the measurements. Samples in the presence of 200µM NH_2OH or 200 µM NO plus 200 µM NH_4^+ were prepared and analyzed in the same way.

References

1   Devol, A. H. Denitrification, Anammox, and N$_2$ Production in Marine Sediments. *Annu. Rev. Mar. Sci.* **7**, 403-423 (2015).

2   Lam, P. & Kuypers, M. M. M. Microbial Nitrogen Cycling Processes in Oxygen Minimum Zones. *Annu. Rev. Mar. Sci.* **3**, 317-345 (2011).

3   Kartal, B., Kuenen, J. G. & van Loosdrecht, M. C. M. Sewage Treatment with Anammox. *Science* **328**, 702-703 (2010).

4   Kartal, B. *et al.* Molecular mechanism of anaerobic ammonium oxidation. *Nature* **479**, 127–130 (2011).

5   Strous, M. *et al.* Deciphering the evolution and metabolism of an anammox bacterium from a community genome. *Nature* **440**, 790–794 (2006).

6   Kartal, B. *et al.* How to make a living from anaerobic ammonium oxidation. *FEMS Microbiol. Rev.* **37**, 428-461 (2013).

7   Maalcke, W. J. *et al.* Structural basis of biological NO generation by octaheme oxidoreductases. *J. Biol. Chem* **289**, 1228-1242 (2014).

8   Putnam, C. D., Arvai, A. S., Bourne, Y. & Tainer, J. A. Active and inhibited human catalase structures: Ligand and NADPH binding and catalytic mechanism. *J. Mol. Biol.* **296**, 295-309 (2000).

9   Auld, D. S. Zinc coordination sphere in biochemical zinc sites. *Biometals* **14**, 271-313 (2001).

10   Moser, C., Chobot, S., Page, C. & Dutton, L. Distance metrics for heme protein electron tunneling. *Biochim. Biophys. Acta* **1777**, 1032-1037 (2008).

11   van de Vossenberg, J. *et al.* The metagenome of the marine anammox bacterium '*Candidatus* Scalindua profunda' illustrates the versatility of this globally important nitrogen cycle bacterium. *Environmental Microbiology* **15**, 1275-1289 (2013).

12   Fulop, V., Ridout, C. J., Greenwood, C. & Hajdu, J. Crystal structure of the di-heme cytochrome-C peroxidase from *Pseudomonas aeruginosa. Structure* **3**, 1225-1233 (1995).

13   Shimizu, H. *et al.* Crystal structure of *Nitrosomonas europaea* cytochrome c peroxidase and the structural basis for ligand switching in bacterial di-heme peroxidases. *Biochemistry* **40** (2001).

14   Echalier, A. *et al.* Redox-linked structural changes associated with the formation of a catalytically competent form of the diheme cytochrome c peroxidase from *Pseudomonas aeruginosa*. *Biochemistry* **47** (2008).

15   Jensen, L. M. R., Sanishvili, R., Davidson, V. L. & Wilmot, C. M. In Crystallo Posttranslational Modification Within a MauG/Pre-Methylamine Dehydrogenase Complex. *Science* **327**, 1392-1394 (2010).

16   Blaschko, H. The mechanism of catalase inhibitions. *Biochem. J.* **29**, 2303-2312 (1935).

17   van der Star, W. R. L. *et al.* An intracellular pH gradient in the anammox bacterium *Kuenenia stuttgartiensis* as evaluated by P-31 NMR. *Appl. Microbiol. Biotechn.* **86**, 311-317 (2010).

References associated with the Methods Section

18   Bendtsen, J. D., Nielsen, H., von Heijne, G. & Brunak, S. Improved prediction of signal peptides: SignalP 3.0. *J. Mol. Biol.* **340**, 783-795 (2004).
19   Brown, P. H. & Schuck, P. Macromolecular size-and-shape distributions by sedimentation velocity analytical ultracentrifugation. *Biophys. J.* **90**, 4651-4661 (2006).
20   Kabsch, W. XDS. *Acta Cryst. Sect. D Biol. Crystallogr.* **66**, 125-132 (2010).
21   Vonrhein, C., Blanc, E., Roversi, P. & Bricogne, G. Automated structure solution with autoSHARP. *Meth. Mol. Biol.* **364**, 215-230 (2007).
22   Schneider, T. R. & Sheldrick, G. M. Substructure solution with SHELXD. *Acta Cryst. Sect. D Biol. Crystallogr.* **58**, 1772-1779 (2002).
23   Abrahams, J. P. & Leslie, A. G. W. Methods used in the structure determination of bovine mitochondrial F-1 ATPase. *A Acta Cryst. Sect. D Biol. Crystallogr.* **52**, 30-42 (1996).
24   Emsley, P. & Cowtan, K. *Coot*: model-building tools for molecular graphics. *Acta Cryst. Sect. D Biol. Crystallogr.* **60**, 2126-2132 (2004).
25   Cowtan, K. D. & Zhang, K. Y. J. Density modification for macromolecular phase improvement. *Progr. Biophys. Mol. Biol.* **72**, 245-270 (1999).
26   Adams, P. D. *et al.* PHENIX: a comprehensive Python-based system for macromolecular structure solution. *Acta Cryst. Sect. D Biol. Crystallogr.* **66**, 213-221 (2010).
27   Murshudov, G. N., Vagin, A. A. & Dodson, E. J. Refinement of macromolecular structures by the maximum-likelihood method. *Acta Cryst. Sect. D Biol. Crystallogr.* **53**, 240-255 (1997).
28   The CCP4 suite: programs for protein crystallography. *Acta Cryst. Sect. D Biol. Crystallogr.* **50**, 760–763 (1994).
29   Petrek, M., Kosinova, P., Koca, J. & Otyepka, M. MOLE: A Voronoi Diagram-Based Explorer of Molecular Channels, Pores, and Tunnels. *Structure* **15**, 1357–1363 (2007).
30   Svergun, D. I. Determination of the regularization parameter in indirect-transform methods using perceptual criteria. *J. Appl. Cryst.* **25**, 495-503 (1992).
31   Svergun, D. I., Petoukhov, M. V. & Koch, M. H. J. Determination of domain structure of proteins from X-ray solution scattering. *Biophys. J.* **80**, 2946-2953 (2001).
32   Pettersen E.F., Goddard T.D., Huang C.C., Couch G.S., Greenblatt D.M., Meng E.C., Ferrin T.E. UCSF Chimera - a visualization system for exploratory research and analysis. *J Comput Chem.* **13**:1605-1612 (2004).

Supplementary Information is linked to the online version of the paper at
www.nature.com/nature.

Authors Contributions

C.F. and W.J.M. isolated the Kuste2859-60-61 complex from *Kuenenia stuttgartiensis*. A.D. and T.R.M.B performed X-ray crystallographic, SAXS and AUC analyses. A.M. performed SAXS measurements. C.F. performed ICP-MS analyses. W.J.M and S. de V. performed EPR sample preparation and analysis. A.D. and T.R.M.B wrote the paper with input from M.S.M.J., J. T. K., S. de V., C.F., W.M. and B.K. The authors declare no conflict of interest. The atomic coordinates and structure factors have been deposited in the Protein Data Bank, www.pdb.org under accession codes 5C2V and 5C2W, respectively.

To whom correspondence should be addressed:

E-mail: Thomas.Barends@mpimf-heidelberg.mpg.de, B.Kartal@science.ru.nl

Extended Data Items

	SAD	Initial Model	Native structure (pdb 5C2V)	Xenon complex (pdb 5C2W)
Data collection[*]				
Space group	*R*32	*R*32	*R*32	*R*32
Cell dimensions				
a, b, c (Å)	461.8, 461.8, 145.1	464.0, 464.0, 145.0	464.5, 464.5, 145.8	464.1, 464.1, 145.1
α, β, γ (°)	90, 90, 120	90, 90, 120	90, 90, 120	90, 90, 120
Resolution (Å)	40-3.4 (3.5-3.4)[†]	40-3.1(3.2-3.1)	40-2.7 (2.8-2.7)	48.5-3.2 (3.3-3.2)
R_{merge}	0.103 (0.530)	0.100 (0.498)	0.096 (0.738)	0.138 (0.641)
$I/\sigma I$	17.8 (3.2)	16.4 (3.7)	18.5 (3.5)	16.6 (4.6)
Completeness (%)	99.9 (100)	99.8 (99.8)	99.8 (100)	100.0 (100.0)
Redundancy	11.7 (8.1)	5.7 (5.6)	8.8 (9.1)	10.6 (10.8)
Refinement				
Resolution (Å)			40-2.7	48.5-3.2
No. reflections			162,788	97,821
R_{work}/ R_{free}			0.235 / 0.271	0.231 / 0.267
No. atoms				
Protein			22,420	22,420
Ligand/ion			344 (8 heme)	344 (8 heme)
			18 (12 Ca, 2 Zn, 2 Mg, 2 Cl)	18 (12 Ca, 2 Zn, 2 Mg, 2 Cl)
			56 (7 betaines)	56 (7 betaines), 4 Xe
Water			500	498
B-factors (Å^2)				
Protein			56.9	71.0
Ligand/ion			58.3	61.4
Water			53.4	57.4
R.m.s deviations				
Bond lengths (Å)			0.009	0.009
Bond angles (º)			1.2	1.3

Extended Data Table 1 | Data collection and refinement statistics.

*Each dataset was collected from a single crystal.

†Highest resolution shell is shown in parentheses.

Data set*	Above Fe-edge	Below Fe-edge	Above Cu-edge
Space group	R32	R32	R32
Unit cell dimensions			
a, b, c (Å)	467.2, 467.2, 146.0	465.3, 465.3, 145.5	465.3, 465.3, 145.5
α, β, γ (°)	90, 90, 120	90, 90, 120	90, 90, 120
Wavelength (Å)	1.73400	1.74600	1.37800
Resolution range (Å) †	30.0-3.80 (3.9-3.8)	30.0-3.50 (3.6-3.5)	30.0-3.20 (3.3-3.2)
Reflections measured	1,165,022 (88,940)	1,469,568 (107,411)	1,995,467 (172,227)
Reflections unique	116,983 (8,703)	147,985 (12,027)	193,705 (17,117)
Completeness (%)	99.9 (99.8)	99.9 (100)	100 (100)
Redundancy N	10.0 (10.2)	9.9 (8.9)	10.3 (10.1)
I/ σI	14.4 (4.7)	18.6 (5.2)	22.2 (6.5)
R_{merge} (%)	15.5 (59.7)	12.6 (50.1)	9.5 (43.6)

Data set	Below Cu-edge	Above Zn-edge	Below Zn-edge
Space group	R32	R32	R32
Unit cell dimensions			
a, b, c (Å)	466.0, 466.0, 146.4	465.0, 465.0, 144.6	465.9, 465.9, 145.0
α, β, γ (°)	90, 90, 120	90, 90, 120	90, 90, 120
Wavelength (Å)	1.38500	1.28100	1.29433
Resolution range (Å) †	30.0-3.40 (3.5-3.4)	40.0-3.50 (3.6-3.5)	40.0-3.80 (3.9-3.8)
Reflections measured	1,669,421 (143,426)	1,465,592 (111,737)	1,134,042 (79,076)
Reflections unique	162,603 (13,535)	147,007 (11,917)	115,562 (8,699)
Completeness (%)	100 (100)	99.9 (100)	99.9 (100)
Redundancy N	10.3 (10.6)	10.0 (9.4)	9.8 (9.1)
I/ σI	17.6 (5.6)	15.4 (3.8)	16.2 (4.6)
R_{merge} (%)	13.1 (55.4)	13.3 (68.3)	13.2 (64.1)

b

| Element/position wrt. absorption edge	Fe/below	Fe/above	Cu/below	Cu/above	Zn/below	Zn/above
Wavelength (Å)	1.746	1.734	1.385	1.378	1.29433	1.281
Energy (eV)	7101	7150	8952	8997	9579	9679
Energy difference from K-edge (eV)	-11	38	-27	18	-80	20
HZS α						
Ca αI	8.1/1.0	6.5/1.0	6.7/1.0	8.8/1.0	6.0/1.0	4.7/1.0
Ca αII	8.7/1.0	4.2/0.6	5.6/0.8	7.7/0.8	4.7/0.8	3.4/0.7
Zn	8.5/1.0	5.7/0.9	4.2/0.6	7.2/0.8	4.5/**0.8**	24.3/**5.2**
Fe Heme αI	4.4/**0.5**	20.3/**3.1**	20.5/3.1	27.4/3.1	17.4/2.9	16.3/3.5
Fe Heme αII	3.8/**0.5**	18.8/**2.9**	18.5/2.8	23.5/2.7	15.3/2.6	12.6/2.7
HZS ß						
Ca ßI	8.9/1.1	6.6/1.0	5.8/0.9	7.9/0.9	4.5/0.8	4.3/0.9
HZS ɣ						
Ca ɣI	9.9/1.2	6./0.90	8.4/1.3	11.2/1.3	6.5/1.1	4.6/1.0
Ca ɣII	8.5/1.0	8.7/1.3	6.8/1.0	8.1/0.9	5.5/0.9	4.6/1.0
Ca ɣIII	12.2/1.5	8.3/1.3	6.8/1.0	11.2/1.3	7.1/1.2	4.6/1.0
Fe Heme ɣI	5.9/**0.7**	17.5/**2.7**	20.4/3.0	27.0/3.1	14.0/2.3	13.8/2.9
Fe Heme ɣII	5.5/**0.7**	16.2/**2.5**	17.6/2.6	23.0/2.6	13.3/2.2	12.9/2.7

Extended Data Table 2 | Identification of metals in hydrazine synthase. a, Data collection statistics for the anomalous diffraction data sets used to identify metal sites in the HZS crystal structure, calculated while considering Friedel mates as individual reflections. *Each dataset was collected from a single crystal, †Highest resolution shell is shown in parentheses. **b**, Heights of peaks in anomalous difference density maps used to identify metal ions. The first number is the observed peak height in σ, the second is the peak height normalized by the height of the anomalous peak at calcium αI for each dataset. Those sites that show a significant difference in normalized peak height below and above an absorption edge are shown in grey. The data confirm the identity of the zinc ion bound to heme αI.
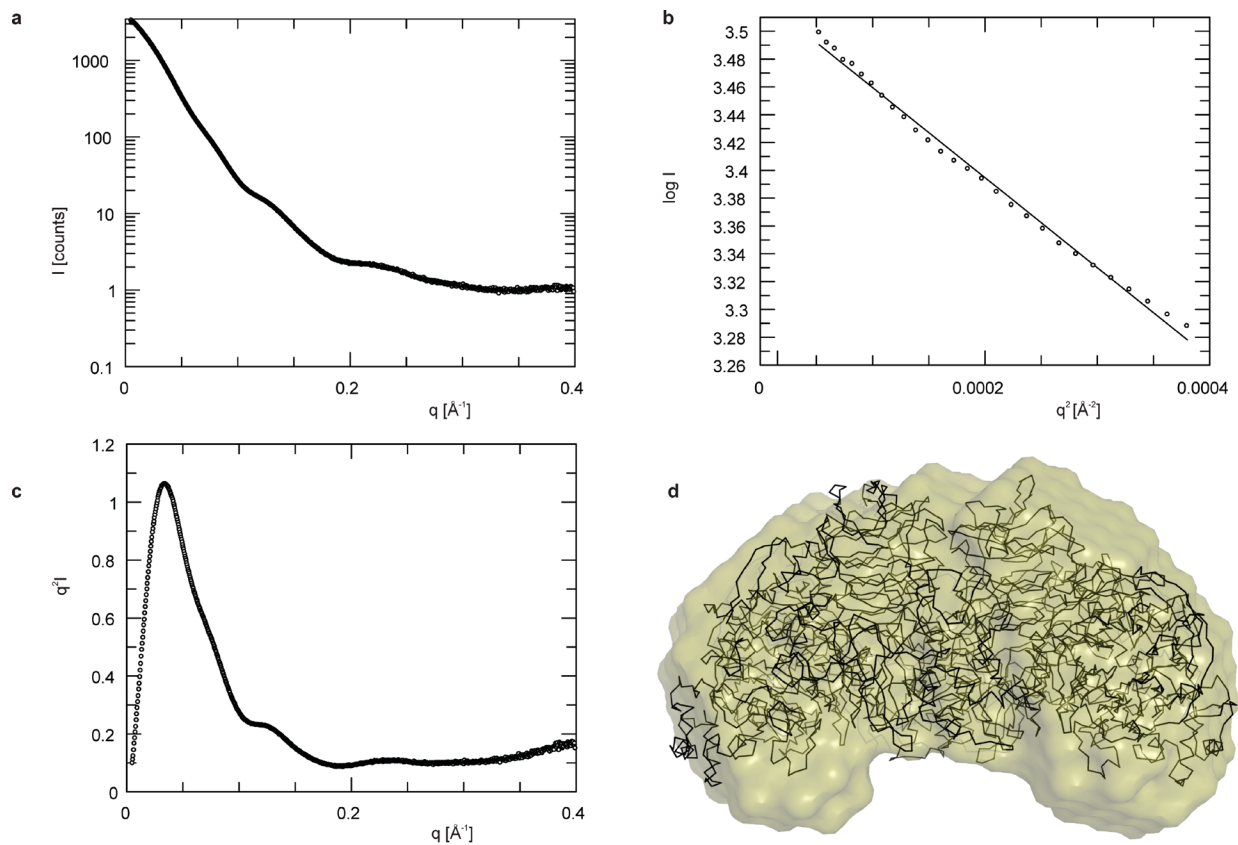
Extended Data Figure 1 | Small-angle X-ray Scattering (SAXS) results. a, Semilogarithmic plot of scattered intensity *I* vs. *q*, which was defined as $q=(4\pi \sin \vartheta)/\lambda$. Features are observed up to $q=0.4$ Å⁻¹. **b,** Guinier plot (plot of *log I* vs. q^2) showing that the protein is not aggregated. **c,** Kratky plot (plot of q^2I vs. *q*) showing that the protein is folded. **d,** Average of 18 (out of 20) dummy-atom reconstructions (beige) overlayed on the crystal structure (black).
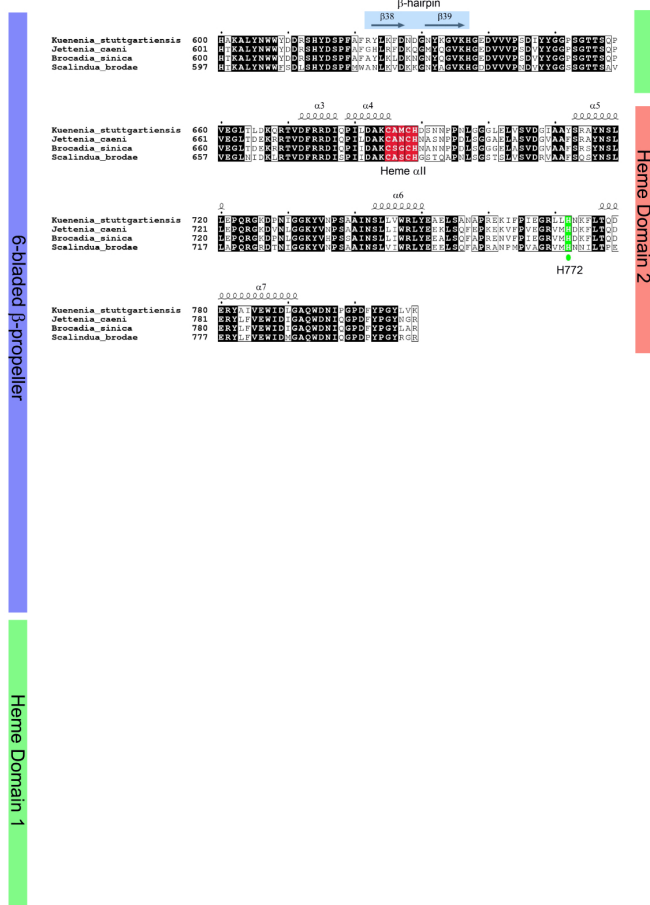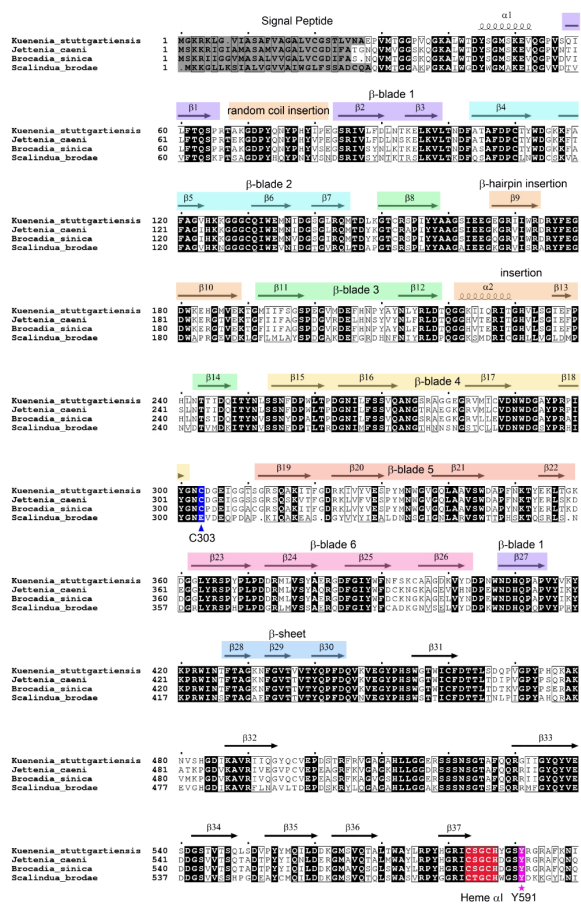
Extended Data Figure 2 | HZS α sequences. The HZS α sequences from *Kuenenia stuttgartiensis* (kuste2861, gi 91200564), *Jettenia caeni* (Planctomycete KSU-1, ksu1d0439, tr A9ZRZ5), *Brocadia sinica* JPN1 (brosiA2676, gi 762182098) and *Scalindua brodae* (scabro01598, gi 726045835, re-confirmed by Sanger sequencing) were aligned in ClustalW [5] and secondary structure elements were manually assigned based on the structure of *Kuenenia* HZS α. Kuste2861 shares 81% sequence identity with its *Jettenia* and *Brocadia* orthologues and 61% with *Scalindua*. Fully conserved peptide sequences are marked black. The predicted signal peptides are highlighted in grey. The following residues are marked (numbering according to kuste2861): Cys303 coordinating to Zn^{2+} (blue triangle), Tyr591 coordinating heme αI (pink star), distal His772 of heme αII (green circle). The *c*-type heme binding motifs are highlighted in red. The figure was prepared using ESPript.
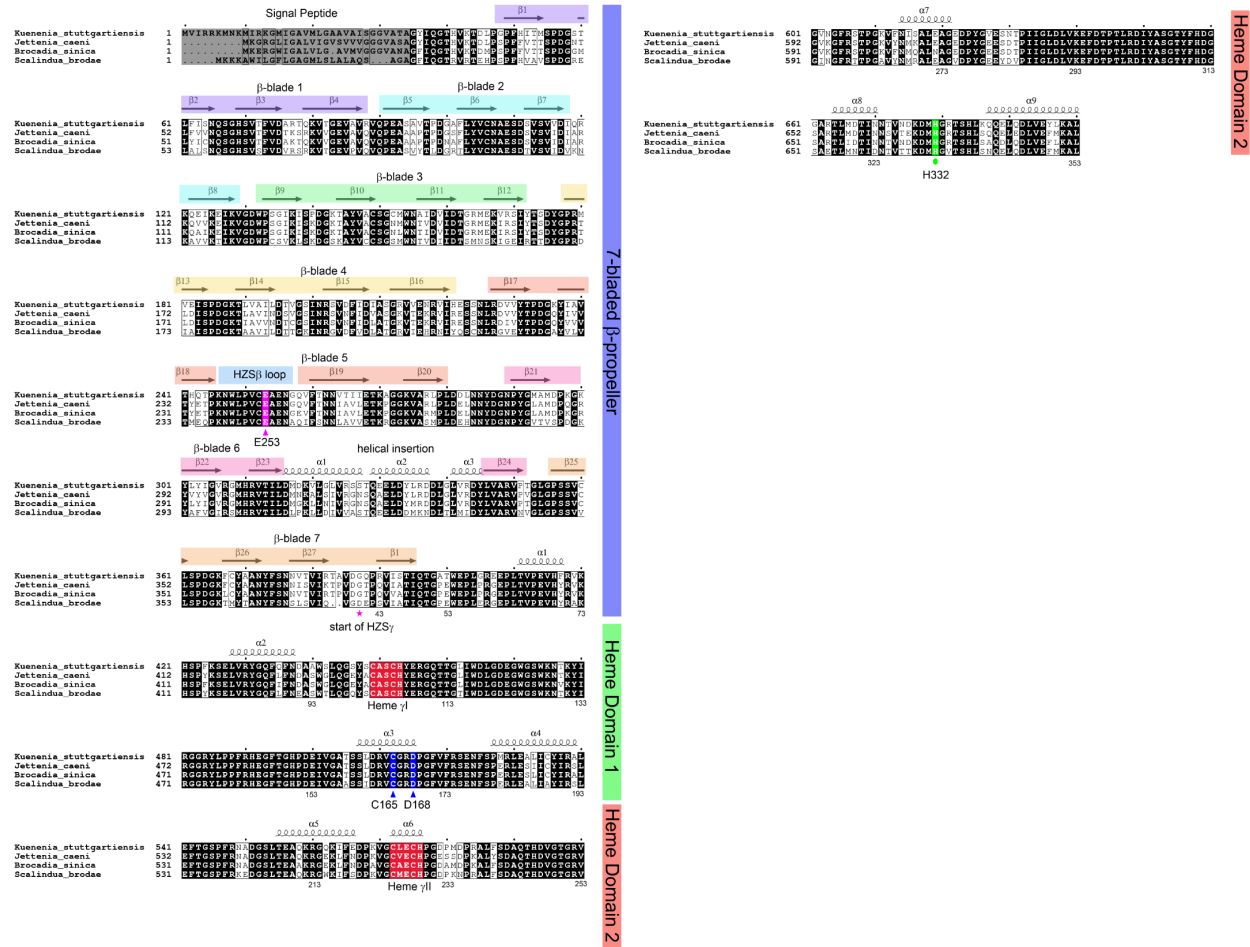
Extended Data Figure 3 | Sequence alignments of HZS β and HZS γ. The HZS βγ fusion protein from *Scalindua brodae* (scabro01046, gi 726046454, re-confirmed by Sanger sequencing) was aligned using ClustalW [5] to the fused sequences of *Kuenenia stuttgartiensis* HZS β (kuste2859, gi 91200562) and HZS γ (kuste2860, gi 91200563, lacking its predicted signal peptide) as well as the to the fused sequences of *Jettenia caeni* (Planctomycete KSU-1) HZS β (ksu1d0441, tr I3IPV5) and HZS γ (ksu1d0440, tr A9ZRZ4, lacking its predicted signal peptide) and the fused sequences of *Brocadia sinica* JPN1 HZS β (brosiA2674, gi 762182096) and HZS γ brosiA2675, gi 762182097, lacking its predicted signal peptide). Secondary structure elements were manually assigned based on the structures of *Kuenenia* HZS β and HZS γ. The first residue of HZS γ in the HZS βγ fusions is indicated by a pink star (starting at residue number 40 of *Kuenenia* HZS γ, the numbers under the *Scalindua* sequence indicate the numbering in kuste2860). The Kuste2859-60 fusion shares 83% sequence identity with its *Jettenia* and *Brocadia* orthologues and 72% with *Scalindua*. Fully conserved peptide sequences are marked black. The predicted signal peptides of the β-subunits are highlighted in grey. The following residues are marked (numbering according to kuste2859 and kuste2860): Glu253 in HZS β (pink triangle), Cys165 covalently bound to heme γI and Asp168 near the heme γI catalytic site (blue triangle) and the distal His332 of heme γII (green circle). The c-type heme binding motifs are highlighted in red. The figure was prepared using ESPript.

The predicted signal peptides of the γ-subunits not included in the alignment are:

23

kuste2860: MAREMRLGGKERMKTGVVKIGLVAALGVVGLISAGGVYA—GQP…
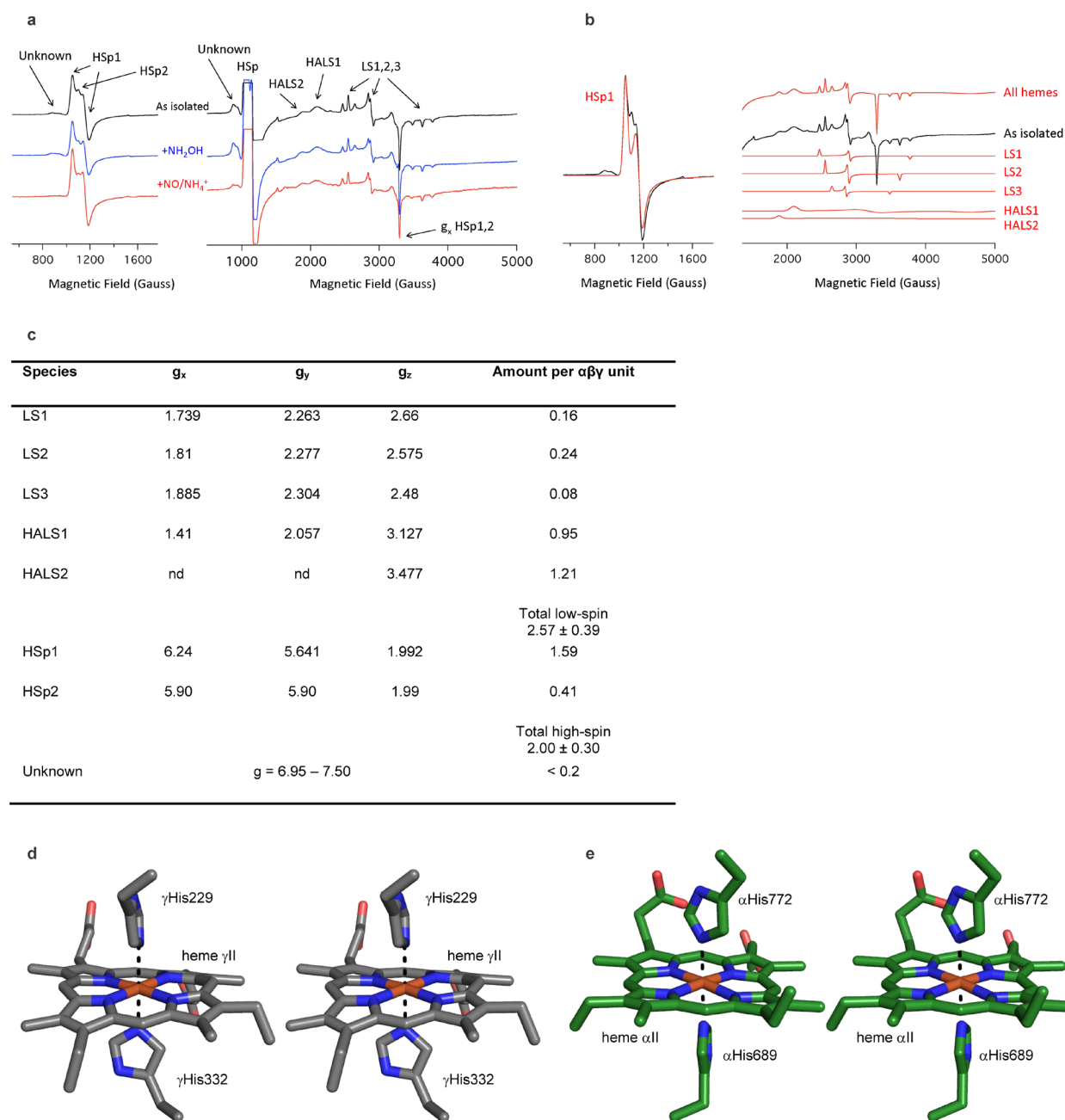
ksu1d0440: MRNGMIKIGLVAALGIAGVVTAGEIMA—GTP…

brosiA2675: MKSSLKIGLIAALGIAGVMTTGELMA—GTP
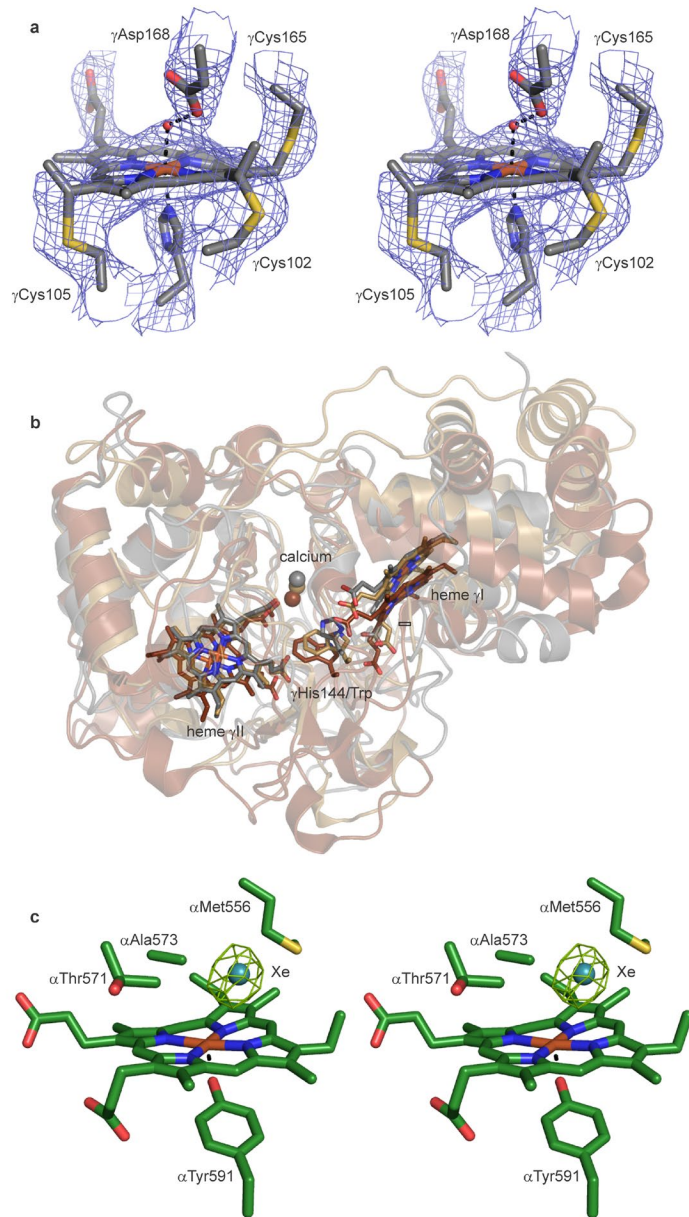
Extended Data Figure 4 | Details of HZS structure. a, Covalent attachment of heme γI *via* three cysteine sulfur atoms. The simulated annealing 2*m*Fo-*D*Fc composite omit map is shown contoured at 1σ, overlaid on the final, refined structure. γCys102 and γCys105 are part of the canonical CXXCH motif, (grey cartoon). In addition, there is a covalent bond between the Sγ atom of γCys165 and the C_1 porphyrin methyl group of heme γI. **b**, Overlay of HZS γ (grey) with *N. europaea* CCP (pdb entry 1IQC, light brown) and *P. denitrificans* MauG (pdb entry 3L4M, dark brown). The positions of hemes γI and γII correspond to those of the hemes in CCP and MauG (sticks), as does the position of a calcium ion (spheres). The conserved tryptophan residue proposed to be involved in redox catalysis in MauG and CCP corresponds to His144 in HZS γ (sticks).**c**, Xenon binding shows that heme αI is accessible from the solvent. The Xe atom is shown as a sphere. Green mesh: *m*Fo-*D*Fc map calculated prior to inclusion of Xe in the model, (10 σ). αMet556 has assumed a new conformation.
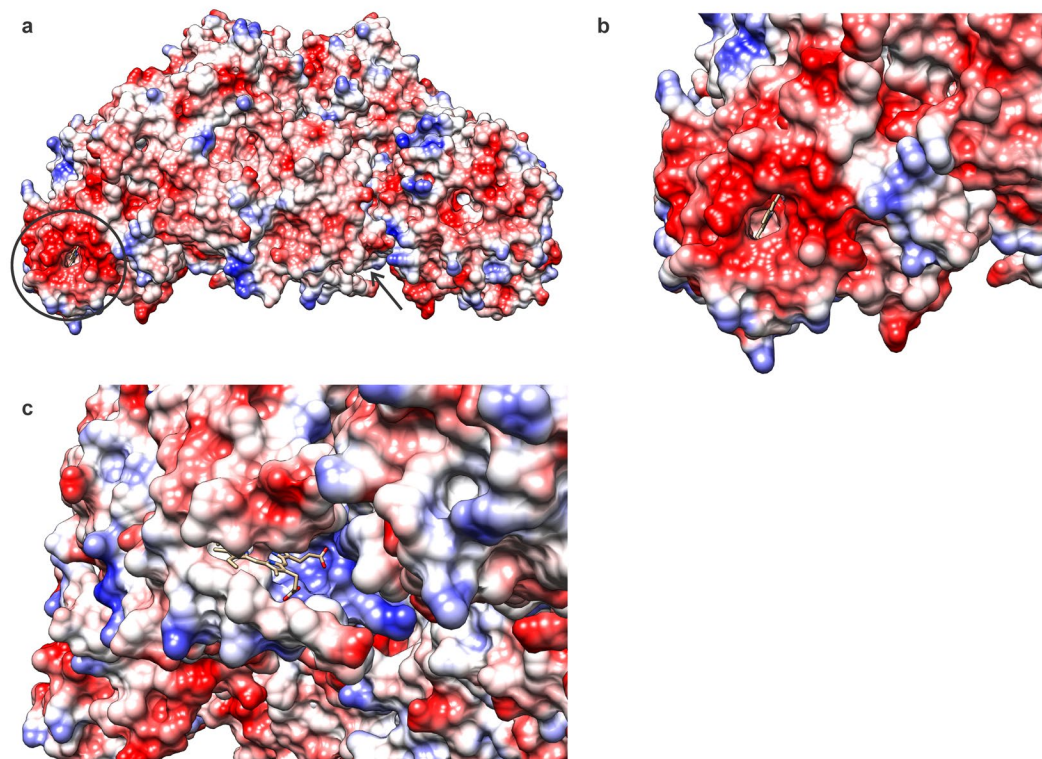
Extended Data Figure 5 | Electrostatic surface properties of the HZS complex. Heme moieties are shown as sticks. **a,** Overview of the whole HZS structure. The bis-His-coordinated heme γII is indicated with a black circle. Heme αII is obscured in this view but its position is indicated by a black arrow. **b**, Close-up view of the electrostatic properties of the surface surrounding heme γII. A prominent negatively charged patch surrounds the heme as in cytochrome C binding sites. **c,** Close-up view of the vacuum electrostatic properties of the surface surrounding heme αII. No significant differences with the rest of the protein surface are observed. Figure prepared using UCSF Chimera[32]. Chimera is developed by the Resource for Biocomputing, Visualization, and Informatics at the University of California, San Francisco (supported by NIGMS P41-GM103311).

a

b

c

Species	g_x	g_y	g_z	Amount per αβγ unit
LS1	1.739	2.263	2.66	0.16
LS2	1.81	2.277	2.575	0.24
LS3	1.885	2.304	2.48	0.08
HALS1	1.41	2.057	3.127	0.95
HALS2	nd	nd	3.477	1.21
				Total low-spin 2.57 ± 0.39
HSp1	6.24	5.641	1.992	1.59
HSp2	5.90	5.90	1.99	0.41
				Total high-spin 2.00 ± 0.30
Unknown		g = 6.95 – 7.50		< 0.2

d

e

Extended Data Figure 6 | EPR spectroscopy of HZS. a, EPR spectra of HZS as isolated (black traces) and after addition of 200μM NH_2OH (blue traces) or 200 μM NO plus 200 μM NH_4^+ (red traces). The left panel shows the low magnetic field region highlighting the high-spin heme g_x and g_y resonances. The right panel shows the complete magnetic field scan where the intensity of the high-spin heme signals has run off-scale. Arrows indicate the positions of the various species that are listed in Supplemental Table S5. The signal at 1540 Gauss is due to a small amount (< 0.2% per αβγ unit) of adventitious iron. **b,** Simulation of the EPR spectra of HZS as isolated using the *g*-values listed in Supplemental Table S5. The difference between the simulation of HSp1 and the experimental spectrum defines the signal of HSp2 and its *g*-value and suggests an amount of 0.41 per αβγ unit (see panel **c**). **c,** HZS heme content per

αβγ unit determined by EPR.*The total heme content determined by EPR was 0.92 ± 0.15 of the optically determined amount. Nd: not detectable. LS: low-spin, HALS: highly anisotropic low-spin, HSp: rhombic high-spin peak. **d,** Stereofigure of the coordination of heme γII by γHis229 and γHis332. The perpendicular orientation of the histidine imidazole rings, both oriented towards heme *meso* atoms, is consistent with the *g*-values for HALS2. **e,** Stereofigure of the coordination of heme αII by αHis689 and αHis772. The orientation of the histidine imidazole groups, one (αHis772) oriented towards a heme nitrogen atom and the other (αHis689) towards a heme meso atom is consistent with the *g*-values for HALS1 (see Supplemental Information).

Supplemental information Dietl *et al.*

Identification of metal ions in HZS

During the course of the refinement of the structure, several large peaks were observed in the electron density maps, which were likely due to metal ions. To ascertain the identity of these metals, several datasets were collected at the PXII beamline of the SLS in Villingen, CH, both above and below the absorption edge of various transition metals (Extended data Table 2a).

Several of the sites were modeled as calcium ions based on the coordination chemistry as well as a lack of significant changes in anomalous difference density maps (the calcium edge is not accessible at most PX beam lines).

After normalizing the remaining peak heights to the peak height of one of the calcium ions (Ca αI), the differences in normalized peak height above and below an X-ray absorption edge can be used to identify the metals by looking for large differences in anomalous difference Fourier maps between data collected above and below the respective absorption edges (Extended data Table 2b).

In this way, the ion bound to the propionate group of heme αI was identified unambiguously as zinc, which is consistent with the coordination chemistry observed in the structure. Moreover, inductively-coupled plasma mass spectrometry (ICP-MS, see methods) confirmed the presence of iron, zinc and calcium in a stoichiometry of Fe:Ca:Zn = 4:8:2 per αβγ heterotrimer, which is comparable to the 4:6:1 stoichiometry observed in the crystal structure. In addition, the conserved βGlu253 residue coordinates a metal ion which was modeled as a magnesium ion because of its typical octahedral coordination sphere and the absence of a peak in the anomalous maps at this position indicative for calcium. Furthermore, the waters around the Mg^{2+}-ion are held in place by the side chains of the conserved αAsn290, βGlu255 and the backbone carbonyl of βCys252.

Mass spectrometry and analytical ultracentrifugation of the hydrazine synthase complex

The following signal peptide cleavage sites were predicted by SignalP:

Kuste2861: MGKRKLGVIASAFVAGALVCGSTLVNA—E^{28}PV…

Kuste2859: MVIRRKMNKMIRKGMIGAVMLGAAVAISGGVATA—G^{35}YI…

Kuste2860: MAREMRLGGKERMKTGVVKIGLVAALGVVGLISAGGVYA—G^{40}QP…

Exact mass determination of the individual subunits by ESI-TOF mass spectrometry confirmed these cleavage sites. The observed mass of the α subunit including bound *c*-type hemes was 88861.07 Da (the calculated mass of kuste2861, starting from residue Glu28 is 88856.1 Da). The observed mass of the β subunit was 38422.50 Da (calculated mass of kuste2859, starting from residue Gly35 is 38420.3 Da), and the observed mass of HZS γ including hemes was 36215.97 Da (calculated mass of kuste2860, starting from residue Gly40, is 36209.9 Da).

Assuming an αβγ heterotrimer with a molecular mass (M) of 163.5 kDa as calculated from the sequences of the individual subunits without signal peptides and including hemes, a maximum possible sedimentation coefficients $S_{max} \approx 0.00361 \times M^{2/3}$ of 10.8, 17.1 and 27.2 can be estimated for αβγ, $\alpha_2\beta_2\gamma_2$ and $\alpha_4\beta_4\gamma_4$ stoichiometries, respectively[1]. As the maximum in the c(S) distribution of HZS was at 11.0 Svedberg (S) corresponding to a $S_{w,20}$ of 11.3 S , these values correspond to $S_{max}/S_{w,20}$ values of 0.96, 1.52 and 2.41, respectively, indicating that HZS most probably occurs as an elongated $(\alpha\beta\gamma)_2$ complex in solution. The experimental sedimentation coefficient corroborated the theoretical value of 13 calculated with HYDROPRO[2] for the HZS $(\alpha\beta\gamma)_2$ complex found in the crystal structure.

Sequence and Mass of the chymotryptic peptide containing methionine sulfoxide M556 determined by MALDI-MS

The mass of the peptide containing αMet556 was determined in the course of determining the identity of the individual subunits (see Methods). The observed mass of the peptide (M^{556}QILDDKGM^{564}SVQTAL) was 1665.79 Da, whereas the calculated monoisotopic mass is 1648.82 Da. The additional mass of 16.97 Da indicates an oxidation of one methionine residue to the corresponding sulfoxide (Met +16 Da). The second methionine in the peptide (M564) is deeply buried in the structure and does not show additional electron density at the sulfur that could be indicative of oxidation.

EPR spectroscopy of HZS.

The X-band EPR spectrum of HZS (Extended Data Figure 6a) shows resonances of isolated rhombic high-spin and low-spin heme centers that can all be simulated (Extended Data Figure 6b) as S_{eff} = ½ or S = ½ systems, respectively, and signals at g = 6.95 - 7.50 with an uncertain origin. Quantitative analyses using the method described in Ref. [3] indicate that the total amount of high-spin and low-spin species are equal within experimental accuracy (Extended Data Figure 6c), which would be consistent with the heme stoichiometry of two bis-His coordinated hemes (αII and γII) and two differently coordinated hemes (αI and γI) per αβγ heterotrimer that is observed in the X-ray structure.

Specifically, the EPR spectrum shows two main highly anisotropic low-spin heme centers (HALS1 and HALS2, Extended Data Figure 6c) in an approximately 1 : 1 stoichiometry as predicted from the X-ray structure. Three additional low-spin heme signals are observed (LS1, LS2 and LS3), which, together represent 0.48 heme per αβγ unit. These latter low-spin signals centers might be derived from 5-coordinated high-spin heme centers that have become 6-coordinated low-spin upon binding of *e.g.* hydroxide. This would be consistent with the observation of a solvent molecule bound to heme γI in the crystal structure, and could also result from a ligated state of heme αI not observed in the crystallographic electron density maps.

The g-value (g_z = 3.47) of the most anisotropic low-spin heme (HALS2) suggests that the two imidazole rings are perpendicular to one another and are both facing a *meso* carbon atom of the porphyrin ring [4]. This is consistent with the arrangement of the two histidines coordinating heme γII (Extended Data Figure 6d). The g-values of HALS1 suggest that the two imidazole rings make an angle of 70° ± 10°, one pointing more towards a *meso* carbon atom, the other to a nitrogen atom of the porphyrin ring [4]. According to the X-ray structure, one of the histidine imidazoles coordinating heme αII lies over N, the other over the *meso* position (Extended Data Figure 6e), a structure quite well in agreement with the g-value for HALS1. Thus, the HALS1 and HALS2 EPR signals can be assigned to hemes αII and γII, respectively. The major rhombic high-spin signal (HSp1) nearly represents 2 hemes (1.59 per αβγ unit, Extended Data Figure 6c) and thus suggests similar EPR spectra and rhombicity for heme 1 in HZS α and heme 1 in HZS γ. The EPR spectrum of HSp1 is consistent with a pentacoordinated heme iron and thus likely corresponds to heme αI. The nature of the minor high-spin heme fraction (0.41, HSp2) cannot be directly assessed, but it could represent a population in which heme αI is coordinated distally by a solvent molecule.

The nature of the signals at g = 6.95 - 7.50 is uncertain. Although high-spin heme centers can have one g-value in this range, the signal appears composed of both an absorbance-like and a derivative-like

feature. A signal with such a line shape, which suggests two g-values considerably greater than 6, cannot originate from an isolated high-spin heme center. It is possible that the signal is derived from an $S = 2$ system, brought about by an antiferromagnetic coupling between a high-spin heme and a low-spin heme center, a suggestion that could be confirmed by parallel mode EPR. Given the long distances between the hemes such a coupling should be mainly dipolar in nature.

The EPR spectra further show that the as-isolated enzyme is completely oxidized. Addition of NH_2OH led to > 80% reduction of HSp2 (Extended Data Figure 6a) without effecting HSp1. Addition of NO plus NH_4^+ led to disappearance of the signals at g = 6.95 - 7.50 and to selective reduction of LS3.

Supplementary References

1   Erickson, H. P. Size and Shape of Protein Molecules at the Nanometer Level Determined by Sedimentation, Gel Filtration, and Electron Microscopy. *Biological Procedures Online* **11**, 32-51 (2009).
2   García de la Torre, J., Huertas, M. L. & Carrasco, B. Calculation of hydrodynamic properties of globular proteins from their atomic-level structure. *Biophysical Journal* **78**, 719-730 (2000).
3   Devries, S. & Albracht, S. P. J. Intensity of highly anisotropic low-spin heme EPR signals. *Biochimica Et Biophysica Acta* **546**, 334-340 (1979).
4   van Lenthe, E., van der Avoird, A., Hagen, W. R. & Reijerse, E. J. Density functional calculations of g-tensors of low-spin iron(I) and iron(III) porphyrins. *Journal of Physical Chemistry A* **104**, 2070-2077, doi:10.1021/jp992959i (2000).